PERGAMON

International Journal of Heat and Mass Transfer 41 (1998) 4121–4138

International Journal of HEAT and MASS TRANSFER

Multiple and unsteady solutions for buoyancy driven flows in spherical annuli

Chandrasekhar Thamire, Neil T. Wright*

Department of Mechanical Engineering, University of Maryland, Baltimore, MD 21250, U.S.A.

Received 10 June 1997; in final form 3 April 1998

Abstract

Results from the analysis of buoyancy driven flows and heat transfer in concentric spherical annuli heated by the inner surface are presented. Crescent eddy flows obtained at low Grashof numbers, Gr, are consistent with published results. Multicellular flows, ranging from steady bicellular to oscillating five-cell flows, are calculated for $Gr_c < Gr < Gr_r$, the specific nature of the flows depending on γ and Gr. For $Gr > Gr_r$, the solution reverts to steady unicellular flows for the radial aspect ratios $\gamma = 0.2$ and 0.25, but with hysteresis for $\gamma = 0.25$. Heat transfer results, given in terms of the local and global Nusselt numbers, illustrate the effect of the flow structures on the heat transfer.

Nomenclature

g^* acceleration due to gravity
Gr' Grashof number based on R_i^* ($Gr' = g^*\beta^*(T_i^* - T_o^*)R_i^{*3}/\nu^{*2}$)
Gr Grashof number based on L^* ($Gr = g^*\beta^*(T_i^* - T_o^*)L^{*3}/\nu^{*2}$)
L^* gap-width ($L^* = (R_o^* - R_i^*)$)
Nu local Nusselt number
Nu_g global Nusselt number
Pr Prandtl number ($= \nu^*/\alpha^*$)
r^* radial coordinate
r scaled radial coordinate
R_i^* radius of the inner sphere
R_o^* radius of the outer sphere
Ra Rayleigh number based on L^* ($Ra = GrPr$)
t^* time
t scaled time
T^* temperature
T scaled temperature
$\mathbf{V}^*$ velocity.

Greek symbols
α^* thermal diffusivity
β^* coefficient of volume expansion
Δ difference in any variable
γ aspect ratio ($\gamma = L^*/R_i^*$)
ϕ azimuthal angle
θ polar angle measured from the upward vertical axis
ρ^* density
ν^* kinematic viscosity
τ scaled time after which the solution converges to time-periodic flows
ψ^* stream function
ψ scaled stream function
ζ^* vorticity
ζ scaled vorticity.

Subscripts
c critical value
g global quantities
i value at inner sphere
o value at outer sphere
r value at reverse transition
t transition value.

Superscript
* dimensional quantities.

1. Introduction

Buoyancy driven flows in concentric spherical annuli with isothermal walls are important for the analysis of

* Author to whom correspondence should be addressed.

0017–9310/98 $19.00
PII: S0017–9310(98)00151–3

heat flow in a number of technically important applications, such as double walled spherical tanks. Many studies have examined these flows, analytically and experimentally. A detailed description of the different experimentally observed flow structures has been given by Bishop et al. [1–3] for air, and Yin et al. [4] for air and water. The flow was observed to be steady as long as the Grashof number, Gr, did not exceed a critical value Gr_c. Exceeding Gr_c led to unsteady, two- or three-dimensional flows depending on the Prandtl number, Pr, and aspect ratio γ. For air, steady unicellular crescent eddy type flows were observed for all γ at low Gr. Transition to a two-dimensional, unsteady falling vortices flow with periodic formation and shedding of vortex cells occurred at $Gr = Gr_c$, for $\gamma = 0.19$ [3]. A similar transition was observed for $\gamma = 0.40$, though with a spiral motion during disruption of the cells and no definite period [4]. For $\gamma = 0.78$ and 1.17, with increasing Gr, the flow first transformed from the crescent eddy to a kidney shaped eddy flow, and then to an unsteady flow with an aperiodic inward radial wave motion and with violent mixing in the central low-speed eddy region. For water, a steady flow with two small like-rotating secondary cells at the top was obtained for all γ, and $Gr < Gr_c$. At $Gr = Gr_c$, this flow changed to an unsteady, falling vortices type of motion for $\gamma = 0.40$, and for $\gamma = 0.78$ and 1.17, a flow with random mixing of the fluid in the region of secondary cells and a relatively stagnant low-speed, primary-cell region. Other experimental studies conducted involved temperature measurements to examine the heat transfer behavior. Bishop et al. [3] presented the measured temperature profiles for air with $\gamma = 0.25, 0.67, 1.0$, and 1.5, and determined the global Nusselt number, Nu_g, as a power function of the Rayleigh number, Ra. For $\gamma = 0.25$ and high Gr, a bicellular flow was observed indirectly from the temperature profile data. Scanlan et al. [5] extended the heat transfer studies to include water and silicone oils, and presented a power-law correlation for Nu_g with $\gamma = 0.09, 0.40, 0.79, 1.18$, and 1.81.

A number of studies have calculated flows in spherical annuli, using a variety of methods and for ranges of Pr and Gr [6–23]. Several conclusions emerge from these studies. Firstly, most studies reproduced the crescent eddy or kidney shaped eddy flow patterns as described by Bishop et al. [1–3] and Yin et al. [4] reasonably well within their respective ranges of Pr and Gr. Secondly, all the studies, except Ingham [11], were restricted to a range of Gr for which only steady flows had been measured in the experimental studies [1–4]. Using over 6400 mesh points, Ingham [11] performed calculations for $\gamma = 0.19$, $Pr = 0.7$, and $Gr \leqslant 2.45 \times 10^5$, a range of Gr larger than that examined by Bishop et al. [3]. In contrast to the experimental results of Bishop et al. [3], which showed the existence of the unsteady falling vortices motion, Ingham obtained steady unicellular flows for all Gr considered. Thirdly, the results of two studies include the existence of steady multicellular flows for $Pr = 0.7$, though at variance with the experimental findings for the range of Gr for a similar range of γ [7, 10]. Mack and Hardee [7] calculated a steady flow with two local secondary counter-rotating eddies, one adjacent to the upward vertical axis and the other adjacent to the downward vertical axis, for $\gamma = 0.15$ and $Gr \approx 1.33 \times 10^4$, but the results came from applying a series expansion beyond the Gr range of validity and did not coincide with the unsteady flows observed for $\gamma = 0.19$ and $Gr > 7 \times 10^3$ [1–3]. Caltagirone [10] calculated a steady bicellular flow with a counter-rotating cell at the top for $\gamma = 0.414$ at $Gr \approx 4.3 \times 10^3$, and $\gamma = 1$ for $7.14 \times 10^3 \leqslant Gr \leqslant 7.14 \times 10^4$, but these results varied from the steady unicellular motion observed by Yin et al. [4] for $\gamma = 0.78$ and 1.17, and $Gr \leqslant 1.5 \times 10^5$. Fourthly, the experimental results seemed to suggest unsteady falling vortices motion at high Gr for $\gamma = 0.19$ and 0.4, but steady bicellular motion for the intermediate $\gamma = 0.25$ at high Gr [1–4]. Finally, the linear stability studies by Douglass et al. [18], Gardner et al. [19], and TeBeest [20] showed that the experimentally observed changes in the flow pattern are due to an instability of the basic motion. The bifurcated flows were calculated to be time periodic and axisymmetric for Pr less than a transition Pr_t and steady and non-axisymmetric for $Pr > Pr_t$.

The range of results from these experimental and numerical studies indicates that much information is not yet available on supercritical convective flows in spherical annuli. This paper provides some new results from a numerical investigation of buoyancy driven flows in spherical annuli for the parameters: $Pr = 0.7$; $\gamma = 0.2$, 0.25 and 0.4; and $Gr \leqslant 10^6$. These ranges permit analysis of the multicellular convection for the three values of γ and the preceding unicellular flows, and enable comparison with the available experimental results. This investigation was motivated by a closely related work in spherical annular sectors by Thamire and Wright, which in turn was motivated by potential medical therapies [21]. The variety of multicellular flows and reverse transitions to unicellular flows calculated there had not been calculated previously and were not compared with empirical results due to a lack of published data for annular segments. The results presented here compare flows in a spherical annulus with published results of measurements and calculations and provide additional information on the evolution of transient flows and multiple solutions for buoyancy driven axisymmetric flows in spherical annuli.

2. Governing equations and numerical scheme

A Boussinesq fluid of $Pr = 0.7$ fills the gap between two concentric spheres (Fig. 1) fixed relative to each other and to an inertial reference frame. The inner and outer spheres are held at uniform temperatures T_i^* and T_o^*

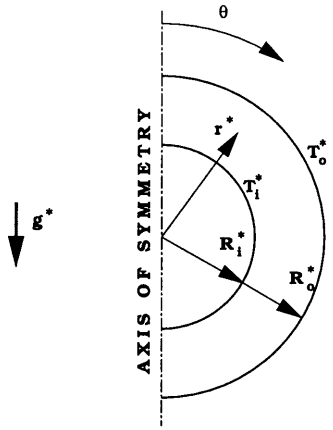

Fig. 1. Enclosure geometry for spherical annuli.

($T_i^* > T_o^*$), respectively, and g* acts downward along the vertical axis. Due to the presumed symmetry of the flows about the vertical axis, the flow field is independent of the longitudinal coordinate ϕ leaving r and θ as the independent spatial variables. The governing Navier–Stokes equations are formulated in terms of a stream function ψ^* that satisfies the mass conservation equation identically, the ϕ-component of vorticity ζ^*, vorticity being the curl of the velocity-vector V^*, and temperature T^*. Scaling length by R_i^*, t^* by R_i^{*2}/α^*, ψ^* by $R_i^*\alpha^*$, $(T^*\text{-}T_o^*)$ by $(T_i^*\text{-}T_o^*)$, and ζ^* by α^*/R_i^{*2} yields

$$\frac{\partial\zeta}{\partial t}-\frac{1}{r^2\sin\theta}\frac{\partial\psi}{\partial\theta}\left(\frac{\partial\zeta}{\partial r}-\frac{\zeta}{r}\right)+\frac{1}{r^2\sin\theta}\frac{\partial\psi}{\partial r}\left(\frac{\partial\zeta}{\partial\theta}-\zeta\cot\theta\right)=-Gr'Pr^2\left(\sin\theta\frac{\partial T}{\partial r}+\frac{\cos\theta}{r}\frac{\partial T}{\partial\theta}\right)+Pr\left(\frac{\partial^2\zeta}{\partial r^2}+\frac{2}{r}\frac{\partial\zeta}{\partial r}+\frac{1}{r^2}\frac{\partial^2\zeta}{\partial\theta^2}+\frac{\cot\theta}{r^2}\frac{\partial\zeta}{\partial\theta}-\frac{\zeta}{r^2\sin^2\theta}\right) \quad (1)$$

$$\zeta=\frac{1}{r\sin\theta}\left(\frac{\partial^2\psi}{\partial r^2}+\frac{1}{r^2}\frac{\partial^2\psi}{\partial\theta^2}-\frac{\cot\theta}{r^2}\frac{\partial\psi}{\partial\theta}\right) \quad (2)$$

$$\frac{\partial T}{\partial t}-\frac{1}{r^2\sin\theta}\frac{\partial\psi}{\partial\theta}\frac{\partial T}{\partial r}+\frac{1}{r^2\sin\theta}\frac{\partial\psi}{\partial r}\frac{\partial T}{\partial\theta}=\frac{\partial^2T}{\partial r^2}+\frac{2}{r}\frac{\partial T}{\partial r}+\frac{1}{r^2}\frac{\partial^2T}{\partial\theta^2}+\frac{\cot\theta}{r^2}\frac{\partial T}{\partial\theta} \quad (3)$$

where r and θ are the scaled radial and polar coordinates respectively, t the scaled time, and Gr' the Grashof number based on R_i. The appropriate boundary conditions for $t > 0$ are

$$\psi=\frac{\partial\psi}{\partial r}=0;\quad T=1\quad \text{at } r=1;$$

$$\psi=\frac{\partial\psi}{\partial r}=0;\quad T=0\quad \text{at } r=1+\gamma$$

$$\psi=\frac{\partial\psi}{\partial\theta}=0;\quad \frac{\partial T}{\partial\theta}=0\quad \text{at } \theta=0,\pi \quad (4)$$

The initial conditions are

$$\psi=0;\quad \zeta=0;\quad T=0\quad \text{at } t=0 \quad (5)$$

The local and global Nusselt numbers (Nu and Nu_g) are defined in terms of T, r, ϕ, and γ as

$$Nu_i=-\frac{\gamma}{1+\gamma}\left.\frac{\partial T}{\partial r}\right|_{r=1};\quad Nu_o=-\gamma(\gamma+1)\left.\frac{\partial T}{\partial r}\right|_{r=1+\gamma} \quad (6(a))$$

$$Nu_{g_i}=-\frac{\gamma}{2(1+\gamma)}\int_0^\pi\left.\frac{\partial T}{\partial r}\right|_{r=1}\sin\theta\,d\theta;$$

$$Nu_{g_o}=-\frac{\gamma(1+\gamma)}{2}\int_0^\pi\left.\frac{\partial T}{\partial r}\right|_{r=1+\gamma}\sin\theta\,d\theta \quad (6(b))$$

where the subscripts i and o denote values at the inner and outer surfaces, respectively.

2.1. Numerical algorithm

Equations (1)–(3) were integrated numerically for conditions (4) and (5), using finite differences. The ADI method [22] was used was used to solve equations (1) and (3) and the SOR method [22] was used for equation (2). At each time-step, the T-field was calculated first, using values of ψ from the previous iteration. Converged solutions for ζ and ψ, along with boundary conditions for ζ, were then obtained using the new T-field. From preliminary analysis, borne out by results, the time-step size was found to be limited by a constraint of the form $\Delta t/((1+R_o)\Delta r\Delta\theta) < c$, with c depending on Gr'. Steady state solutions were considered converged when the maximum change in the local values of each variable and in each of the global energy rates at the spherical surfaces became less than 10^{-4} percent. For the periodic solutions, calculations were performed for at least 20 periods of oscillation. The global energy rates at the spherical surfaces were required to be within 1% of each other for conservation of energy. The grid size was refined when any of these requirements was not satisfied. The global energy rates were within 0.25% of each other for the majority of the computations, the maximum difference that occurred being 1.2% for $Gr = 3.2\times10^5$ and $\gamma = 0.4$ using a grid size of 161x51. Calculations had to be restricted to $Gr \leqslant 3.2\times10^5$ for this γ, as further grid refinement

was needed for higher Gr, which in turn required excessive computer times. Usually, fewer than 5600 grid points were used, except to test convergence and accuracy. Grid independence was rigorously checked for representative calculations, especially for those where changes in the flow patterns took place. While for the unicellular flows grid independence was achieved at relatively coarse grid sizes, finer grid sizes, especially in the θ-direction, were needed for multicellular flows and at reverse transitions. For instance, for $\gamma = 0.25$ and $Gr = 4.5 \times 10^3$, while grid sizes of 61×21, 61×26, 71×21, 71×26, 81×21, 81×26, 91×21, 91×26, and 101×21 produced unicellular flow solutions, 101×26, 121×21, 121×26, 126×26, 136×26, 151×21, 151×26, 151×31, 181×21, 181×26, and 181×31 produced time-periodic flow solutions, with grid independence of Nu_g being achieved after 3276 grid points.

Results of the code for $Pr = 0.7$, $Ra = 1000$ and $\gamma = 1$ compared favorably with the analytical results of Mack and Hardee [7], and for $Pr = 0.7$ and $\gamma = 0.19$ with the experimental results of Scanlan et al. [5], as noted in Thamire and Wright [24]. Below, results from the present calculation are compared further with those of Scanlan [5]. To facilitate comparison with earlier work, the current results are presented using a different scaling form than that used to perform the integration, i.e. Gr based on L^* is used in place of Gr' based on R^*, and t^* is rescaled by L^{*2}/α.

3. Results and discussion

3.1. Flows and isotherms for $\gamma = 0.2$

Flows calculated for $\gamma = 0.2$ and $Gr \leqslant 1.6 \times 10^5$ are essentially of three types, after the initial transient: steady unicellular, oscillatory multicellular, and steady multicellular. Unicellular flows are computed for $Gr < 4.8 \times 10^3$ and $Gr \geqslant 3.2 \times 10^4$, while multicellular flows are calculated for intermediate values of Gr. Sample flow patterns are shown in Fig. 2, with the isotherms on the left side and streamlines on the right.

Flows for $Gr < 4.8 \times 10^3$ (Fig. 2(a)) are the crescent eddy type [1–4], characterized by the formation of a distinct crescent eddy of slow moving fluid in the central portion of the cavity, surrounded by thin layers of rapidly moving fluid adjacent to the spherical surfaces. The warm fluid rises upward along the inner sphere, forms a plume near $\theta = 0$, descends rejecting heat to the cold outer sphere, and returns to the lower central axis, forming a recirculation ring that fills the entire cavity. As Gr increases, the flow velocities increase, and the center of the eddy moves slightly towards $\theta = 0$. The isotherms at low Gr correspond closely to the conduction solution, but begin to deform as Gr increases. A sharp radial temperature occurs near the bottom of the inner surface. With decreasing θ, the isotherms spread with the decreasing radial gradients. For the cooler outer sphere, the isotherms are packed closely near the top, but spread as θ increases. At the $\theta = 0$ and π symmetry boundaries the isotherms are normal to the vertical axis. In the low-speed core, relatively small temperature gradients exist, as the isotherms illustrate.

At $Gr = 4.8 \times 10^3$, the flow changes to a time-periodic multicellular pattern (Fig. 2(b)), as the flow changes periodically from bicellular to quadcellular and back. Shown in the inset of Fig. 2(b) is Nu_g as function of t, τ being an arbitrary time after the flow has settled into its periodic motion; Nu_g illustrates the global effect of the flow structure on the heat transfer. The streamlines and isotherms shown correspond to the circled point of the Nu_g history plot and portray a four-cell state that exists only during a portion of the circled peak of the Nu_g curve. Throughout the cycle, the cells oscillate in the θ-direction. The isotherms exhibit periodic temperature–gradient reversals, in accordance with the flow reversal occurring at adjoining faces of the cells. As Gr increases, the portion of the period during which the four-cell state exists increases, with increasing differences in Nu_g between the four-cell and bicellular flows (Fig. 2(c)). As Gr increases to 8×10^3, a fifth cell appears in a flow pattern similar to that described above, but with the flow regularly changing from three to five cells and back in each period. The flow velocities increase with increasing Gr, and the isotherms in the primary cell become stably stratified. At $Gr = 9.6 \times 10^3$, the period of oscillation between three and five cells nearly doubles from that at the onset, but with no qualitative macroscopic effect except for increasing the duration of the five-cell state, which is consistent with the trend calculated thus far, for increasing Gr.

For $1.48 \times 10^4 \leqslant Gr < 1.68 \times 10^4$, a steady five-cell pattern occurs (Fig. 2(d)). Fluid in the top two cells and the fourth cell (from top) is isolated from the rest of the fluid, but the third and primary (fifth) cells are connected by the radial gap between the outer sphere and the fourth cell through which small amount of fluid flows. Crowding of the isotherms occurs at five regions in the top, increasing the local heat transfer rates in those areas. As Gr increases further, an oscillatory five-cell pattern occurs for $1.68 \times 10^4 \leqslant Gr < 1.95 \times 10^4$, with periodic movement of the fluid in both r- and θ-directions. A falling vortices type of flow occurs next, for $1.95 \times 10^4 \leqslant Gr < 3.2 \times 10^4$, which periodically changes from a unicellular to tricellular state; Fig. 2(e) shows such a flow for $Gr = 2 \times 10^4$ [1–4]. Within each period, beginning with a unicellular state, a secondary cell is generated at the top of the annulus, which almost immediately breaks into two cells. The first cell then expands, accompanied with shrinking of the second cell. In the Nu_g history plot, this process corresponds to the steeply rising portion of the curve. Oscillations in Nu_g then occur, corresponding to the second cell alternately enlarging and shrinking, allowing

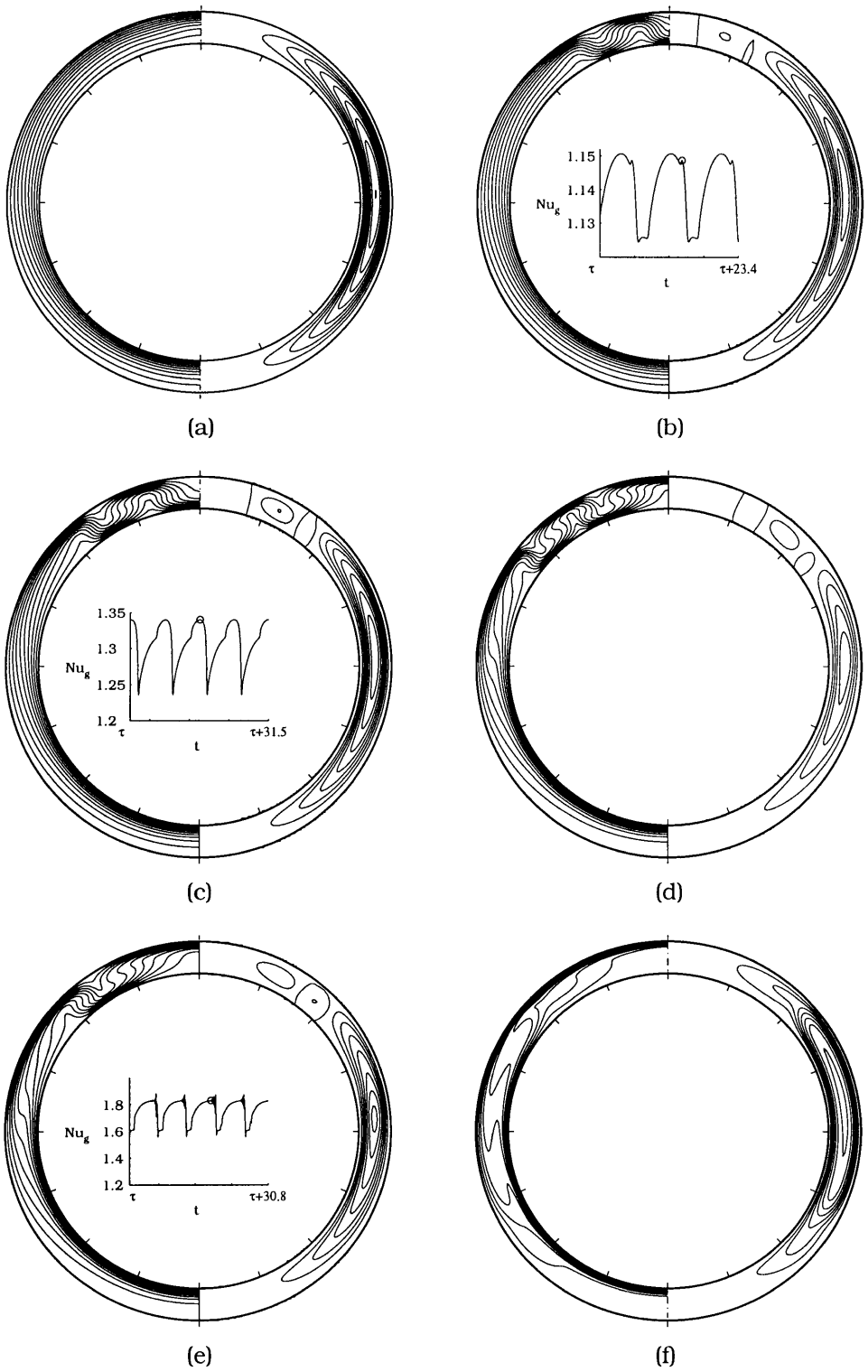

Fig. 2. Flow patterns for $\gamma = 0.2$ and $Gr =$ (a) 4.7×10^3 ($\Delta\psi = -1$); (b) 4.8×10^3 ($\Delta\psi = -1.4$); (c) 7.4×10^3 ($\Delta\psi = -1.75$); (d) 1.6×10^4 ($\Delta\psi = -5$); (e) 2×10^4 ($\Delta\psi = -4$); (f) 1.6×10^5 ($\Delta\psi = -10$).

fluid to intermittently pass between the top and primary cells through the radial gap generated between the outer sphere and second cell. There appears to be a stage when the heat transfer attains its maximum value (corresponding to the maximum displacement of the second cell in the θ-direction, while it occludes the flow between the top and bottom cells), at which point the flow collapses and all four cells merge into one elongated cell, resulting in a momentary inversion to the unicellular state. This state lasts only for a fraction of the period before breaking into two cells, as before. At $Gr = 3.2 \times 10^4$ the flow reverts to a unicellular pattern (shown in Fig. 2(f) for $Gr = 1.6 \times 10^5$), after exhibiting the transient falling vortices type of behavior which diminishes rapidly after two periods of oscillation. Further calculations for Gr up to 1.6×10^5 produced no qualitative changes in the flow, except for the increasingly boundary-layer character of the flow and the stable stratification of the isotherms in the core.

3.1.1. Transient flows

Figure 3(i) shows the time evolution from quiescence of Nu_g for a typical periodic flow ($Gr = 9.6 \times 10^3$) and Fig. 3(ii) shows the streamlines and isotherms corresponding to points B, E, F, and H of the Nu_g curve. When Gr is increased from 0 to 9.6×10^3 over a time $t \approx 0.6$, a unicellular flow develops which remains unicellular until $t \approx 7.7$, when a secondary cell develops at the top. Expanding in the θ-direction, this cell breaks into two more cells at $t \approx 8.6$ and the flow then settles into a steady periodic motion with a period approximately equal to 10.9. In a typical cycle, the flow changes from three to five cells and then back to three, the changes occurring mainly in the top one-third of the annulus. In the tricellular flow (point A of Fig. 3(i)), the top cell expands in the θ-direction (Fig. 3(ii–a), point B) until point C, when a fourth cell is generated at the top. This cell then expands (Fig. 3(ii–b), point E), the third cell shrinking in the process. A fifth cell appears at point E and expands, displacing the fourth cell in the θ-direction, the second and third cells correspondingly shrinking (Fig. 3(ii–c), point F). The second cell then begins shrinking, first in the r-direction, and then in the θ-direction, and eventually disappears (Fig. 3(ii–d), point H), while the top cell continues to expand. The bottom two cells then merge with each other and the flow returns to the three-cell state. The isotherms throughout the cycle exhibit crowding at different places in accordance with the changes in the flow pattern, affecting the local heat transfer in the top portion; the bottom two-thirds of the annulus remain nearly unaffected. The maximum in Nu_g occurs in a five-cell state with flow occurring between the third and bottom cells through the gap above the second cell.

3.2. Flows and isotherms for $\gamma = 0.25$

Flows calculated for $\gamma = 0.25$ also exhibit two transitions; the multicellular flows calculated in between the two transitions, though, are steady flows occurring in wider ranges of Gr than for $\gamma = 0.2$. Unicellular flows occur for $Gr < 3.7 \times 10^3$ and steady bicellular flows for $3.7 \times 10^3 \leqslant Gr < 4.5 \times 10^3$ (Fig. 4(a)), followed by a periodic flow at 4.5×10^3. As described above, expansion and contraction of the cells in both θ- and r-directions occurs with the flow changing from unicellular to tricellular in each period (shown in Fig. 4(b) for $Gr = 4.7 \times 10^3$). As Gr increases slightly, the flow begins to oscillate from bicellular to tricellular in each period. At $Gr = 6 \times 10^3$, another periodic flow pattern occurs that changes from bicellular to tricellular to quad-cellular, the tricellular being of the longest duration, compared to the other two states. As Gr further increases, a steady tricellular flow occurs for $8.2 \times 10^3 \leqslant Gr < 1.5 \times 10^4$ (Fig. 4(c)), which changes to an oscillatory tricellular flow at $Gr = 1.5 \times 10^4$. With further increase in Gr an oscillatory four-cell pattern results for $1.61 \times 10^4 \leqslant Gr < 1.9 \times 10^4$ (Fig. 4(d)). Then, a falling vortices type of flow pattern occurs for $1.9 \times 10^4 \leqslant Gr < 2.65 \times 10^4$ (Fig. 4(e)). The period of the motion increases by an order of magnitude, but decreases nearly linearly with increasing Gr. A reverse transition to unicellular flows occurs at $Gr = 2.65 \times 10^4$. Further increase in Gr causes thinning of the boundary layers and increasingly stable stratification of the isotherms (Fig. 4(f)).

3.2.1. Transient flows

With Gr increased to 1.56×10^4 within $t = 0.11$, the flow passes through unicellular (Fig. 5(ii–a), point A of Fig. 5(i)) and bicellular (Fig. 5(ii–b), point B) flows first. A tricellular flow next occurs along the curve BC, and for a very brief period, a quad-cellular state (Fig. 5(ii–c), point C) corresponding to the small peak at C. The flow reverts to a tricellular flow almost immediately, with all three cells separated. At point D, the second cell shrinks in the r-direction, creating a radial-gap at its top, allowing fluid exchange between the top and bottom cells. This state remains steady for $t \approx 11$, after which fluctuations of constant amplitude in Nu_g develop corresponding to the shrinking and enlarging of the second cell (Fig. 5(ii–d), point E).

At $Gr = 2.65 \times 10^4$, the long term solution reverts to a steady unicellular flow. If Gr is increased to 2.65×10^4 in $t = 0.9$, the transient response is illustrated in Fig. 6 for an initially quiescent fluid. A unicellular flow persists up to point A of Fig 6(i). The flow changes to a bicellular flow at point A, and to a tricellular flow at point B. A fourth cell develops almost immediately, and shrinking and expanding of the second cell (Fig. 6(ii–a), point C) occurs with increasing amplitudes, causing the Nu_g to

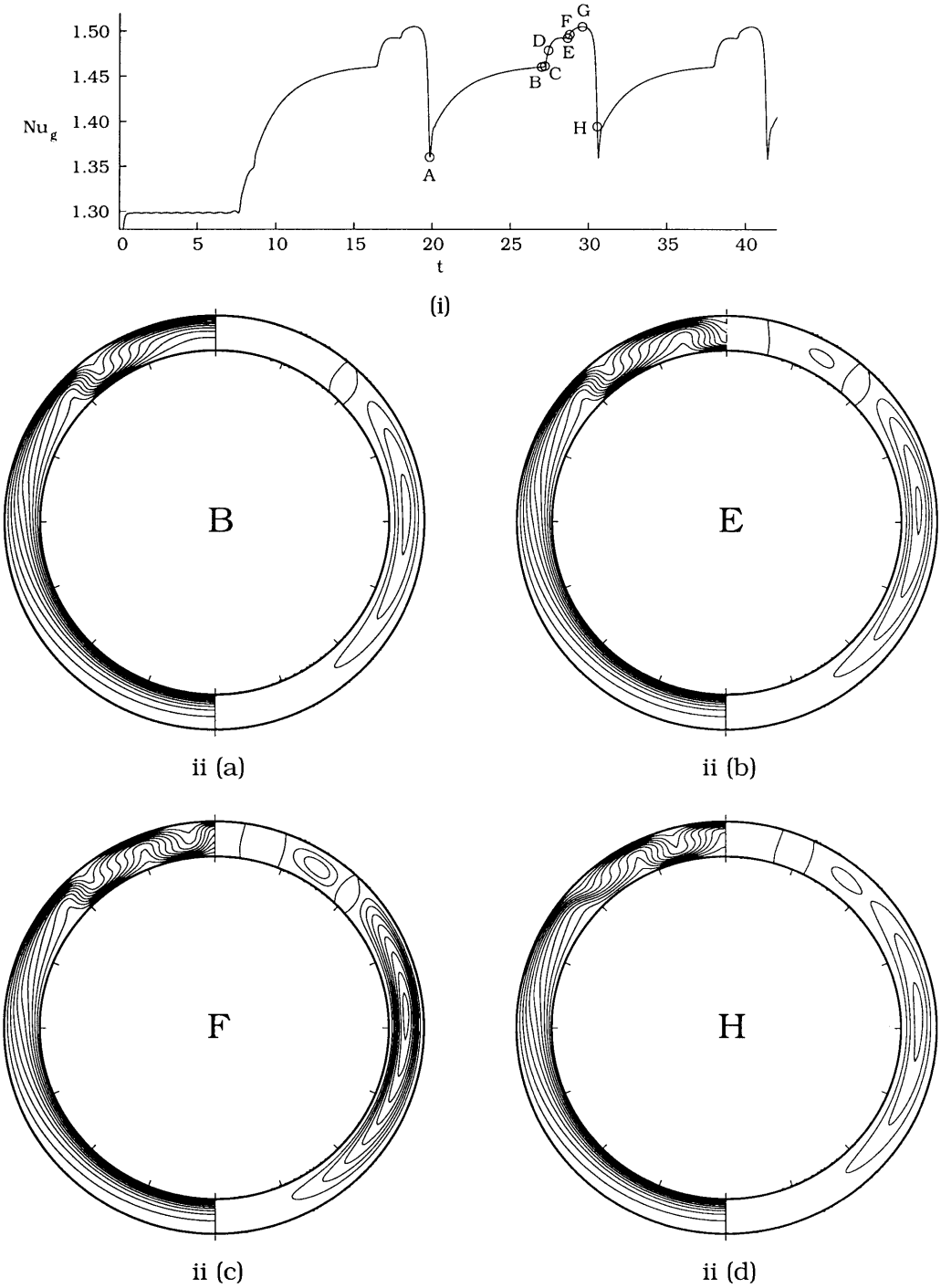

Fig. 3. (i) Nu_g history curve for $Gr = 9.6 \times 10^3$, $\gamma = 0.2$; (ii) flow states corresponding to points B, E, F, and H of (i).

oscillate in time. The second cell eventually disappears, and the third and bottom cells combine to form a bicellular flow corresponding to point D of Fig. 6(i). The top cell then expands (Fig. 6(ii–b), point E), and a third cell is generated at the outer surface corresponding to the small valley near point E. This cell grows accompanied

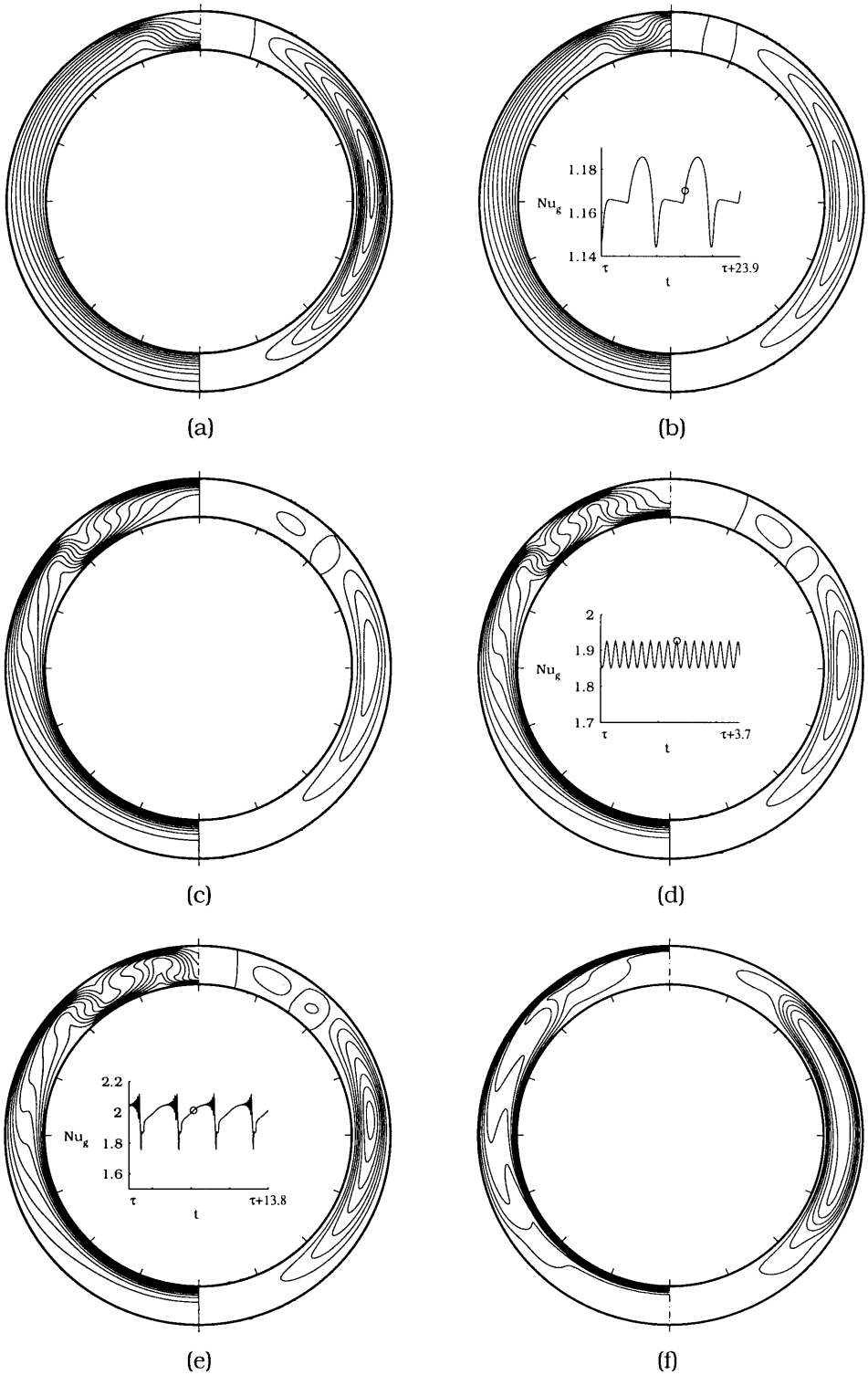

Fig. 4. Flow patterns for $\gamma = 0.25$ and $Gr =$ (a) 4.3×10^3 ($\Delta\psi = -1$); (b) 4.7×10^3 ($\Delta\psi = -2$); (c) 1.25×10^4 ($\Delta\psi = -5$); (d) 1.76×10^4 ($\Delta\psi = -5$); (e) 2.34×10^4 ($\Delta\psi = -4$); (f) 2.08×10^5 ($\Delta\psi = -10$).

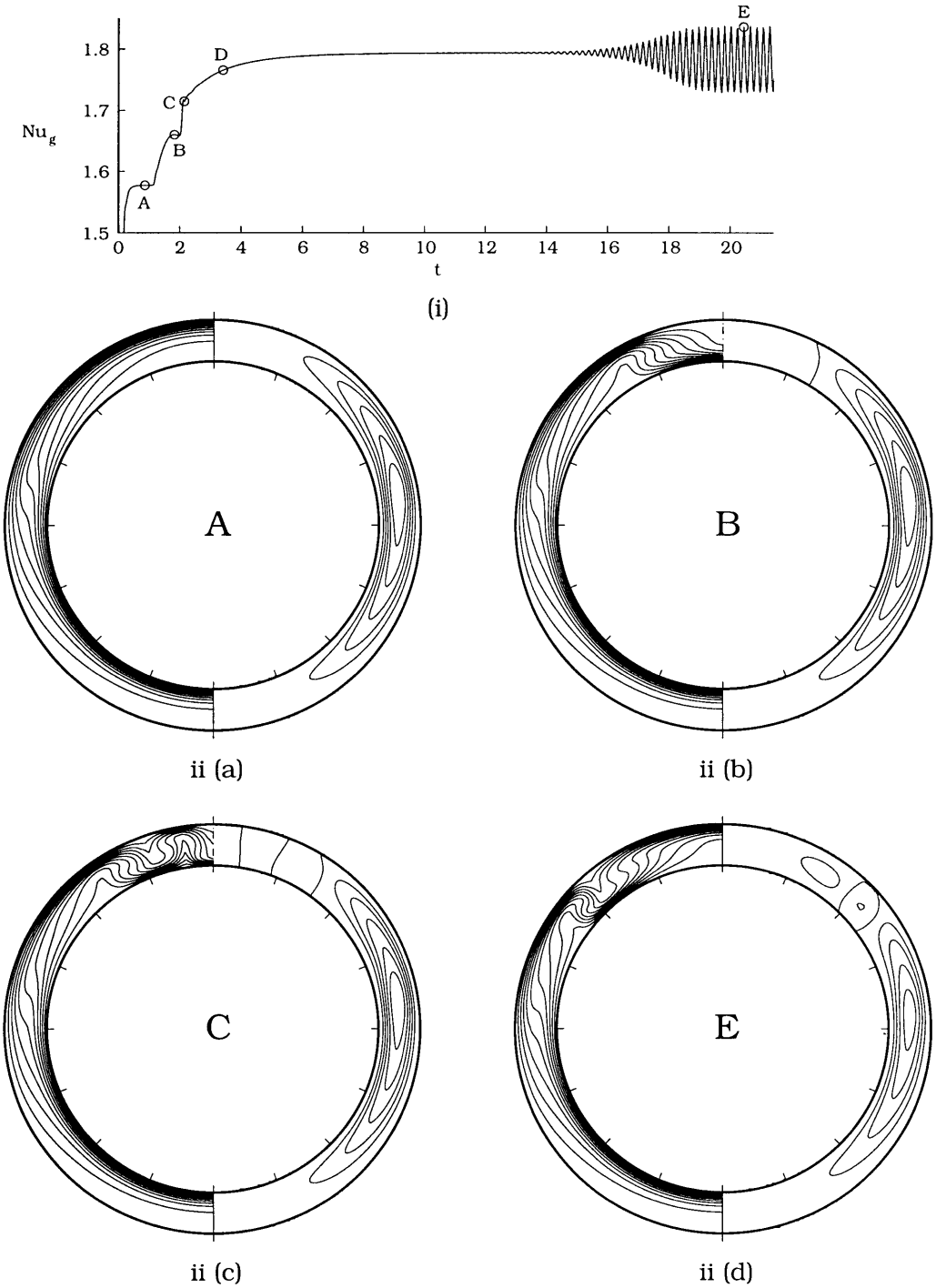

Fig. 5. (i) Nu_g history curve for $Gr = 15.625 \times 10^3$, $\gamma = 0.25$; (ii) flow states corresponding to points A, B, C, and E of (i).

by shrinking and stretching of the second cell and oscillations in Nu_g (Fig. 6(ii–c), point F), until the second cell becomes too small and the top and bottom cells combine to form an elongated cell. This cell soon changes into a crescent eddy type of cell, and the flow becomes a stable, steady, unicellular flow (Fig. 6(ii–d), point G).

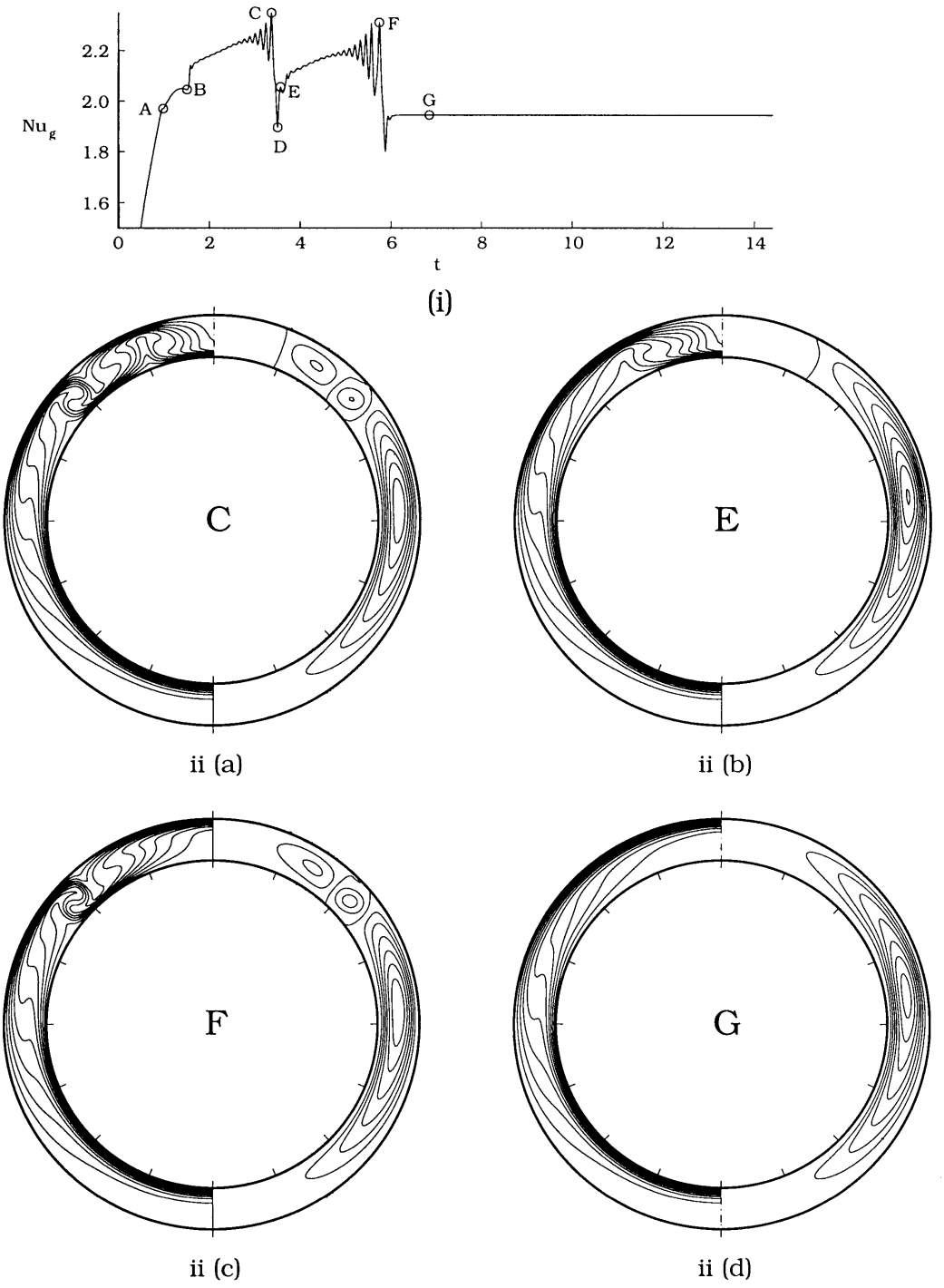

Fig. 6. (i) Nu_g history curve for $Gr = 2.65 \times 10^4$, $\gamma = 0.25$; (ii) flow states corresponding to points C, E, F, and G of (i).

3.3. Flows and isotherms for $\gamma = 0.4$

Flows calculated for $\gamma = 0.4$ are composed only of steady unicellular and unsteady falling vortices regimes. Crescent eddy unicellular flows are obtained for $Gr < 6.9 \times 10^4$; at $Gr = 6.9 \times 10^4$, a periodic falling vortices type motion occurs, with the flow cyclically changing from a unicellular flow to a tricellular flow. Oscillations in Nu_g occur in the tricellular state corresponding to shrinking and enlarging of the second cell. With increasing Gr, these changes occurring in the second cell become confined to a small portion at the beginning of the period; for the majority of the period, a small radial gap at the bottom of the second cell occurs through which there is some flow connecting the top and bottom cells (Fig. 7(a)). At $Gr = 1.25 \times 10^5$, aperiodic falling vortices flows occur with the top two cells deforming to varying magnitudes in each cycle and causing aperiodic oscillations in Nu_g (shown in Fig. 7(b) for $Gr = 1.44 \times 10^5$). At $Gr = 1.6 \times 10^5$, the flow becomes nearly steady-periodic again. With further increase in Gr, the primary cell begins to exhibit characteristics of the boundary layer regime; the boundary layers become thin, isotherms are stratified in the core, and two or more like rotating cells appear in the core. Figure 7(c) shows such a flow for $Gr = 2.88 \times 10^5$. Increasing Gr further causes aperiodic flows (Fig. 7(d)) again, which persist up to $Gr = 3.2 \times 10^5$, the maximum Gr examined for this γ. The period of the motion (averaged over ten cycles, for the aperiodic flows) steadily decreases from 1.6 to 0.4, except for a small peak at $Gr = 1.15 \times 10^5$.

3.3.1. Transient flows

The evolution of a typical periodic falling vortices flow from quiescence to $Gr = 7.36 \times 10^4$ in $t = 0.03$ is shown next in Fig. 8. Figure 8(ii–a) shows the tricellular flow at point A of Fig. 8(i); the high velocity boundary flow occurs through the radial gaps at the second cell. The second cell then grows and occludes the flow between the top and bottom cells (Fig. 8(ii–b), point B); Nu_g here is at its maximum. The top two cells then merge together (Fig. 8(ii–c), point C), followed by merging with the primary cell, forming one elongated cell (Fig. 8(ii–d), point D), which shifts towards $\theta = 0$. This elongated cell quickly breaks into two cells (Fig. 8(ii–e), point E), and then more cells (Fig. 8(ii–f), point F). The first cell then grows both in r- and θ-directions, and the second in the θ-direction. As the top two cells grow, velocities continue to increase, and the second cell begins to expand and contract until all three cells merge together again, and the periodic motion continues.

3.4. Hysteresis

Each of the flows described so far has been calculated starting from the quiescent state, given by equation (5). The observation of stepwise changes of Nu_g corresponding to forward and reverse transitions in the present study, coupled with the well-known possibility that the non-linear Navier–Stokes equations may possess multiple solutions for some values of parameters, suggests the possibility of multiple solutions here. Moreover, comparing the results of past analyses [7, 10, 11] to the experimental study by Bishop et al. [3] and from the computations of multiple solutions for the spherical annular sectors [24], it appears that at least two solutions may exist for the same Gr for flows in spherical annuli as well.

To examine the existence of multiple solutions, a second set of initial conditions was used and computations were performed for Gr between Gr_c and the Grashof number of the reverse transition from multicellular to unicellular flow, Gr_r. Practically, the temperature of the inner sphere may be increased beyond the reverse transition and then decreased in potential medical applications. Thus, one of the converged solutions obtained for $Gr > Gr_r$ using equation (5) was used as initial condition for calculating a second set of solutions for $Gr_c \leqslant Gr \leqslant Gr_r$. For $Gr < Gr_c$, a solution obtained for $Gr_c < Gr < Gr_r$ using equation (5) was used as the second initial condition. The flows remained unchanged from the previous ones for $\gamma = 0.2$. For $\gamma = 0.25$, however, a second set of solutions, accompanied by hysteresis in Nu_g, were found for $Gr < Gr_r$. For $Gr_c \leqslant Gr \leqslant Gr_r$ (recall $Gr_c = 3.7 \times 10^3$ and $Gr_r = 2.65 \times 10^4$), these solutions are steady unicellular flows, and for $3.04 \times 10^3 < Gr < Gr_c$, steady bicellular flows. No change was found in the solutions for any other Gr. It is thus clear that depending on γ, at least two domains of Gr exist, one for which the flow structure due to steady boundary conditions is dependent on the initial conditions, and one for which it is independent of initial conditions. Of the two sets of solutions, those yielding multicellular flows are found to be associated with higher Nu_g, as described below. For $\gamma = 0.4$, since calculations for Gr large enough to produce a reverse transition were not performed, the converged solution for $Gr = 3.2 \times 10^5$ was used as the second initial condition. These calculations produced no new solutions and did not produce any hysteresis.

3.5. Heat transfer results

3.5.1. Global Nusselt numbers

Figure 9 compares the influence of multicellular flows on Nu_g and the correlation given by Scanlan et al. [5]. Dashed lines on either side of the solid curve represent the maximum and minimum values of Nu_g within each period for the periodic flows (averaged over ten periods for aperiodic unsteady flows), and the solid line, the mean value. Clearly, multicellular flows have a larger Nu_g compared with corresponding unicellular flows. For $\gamma = 0.2$

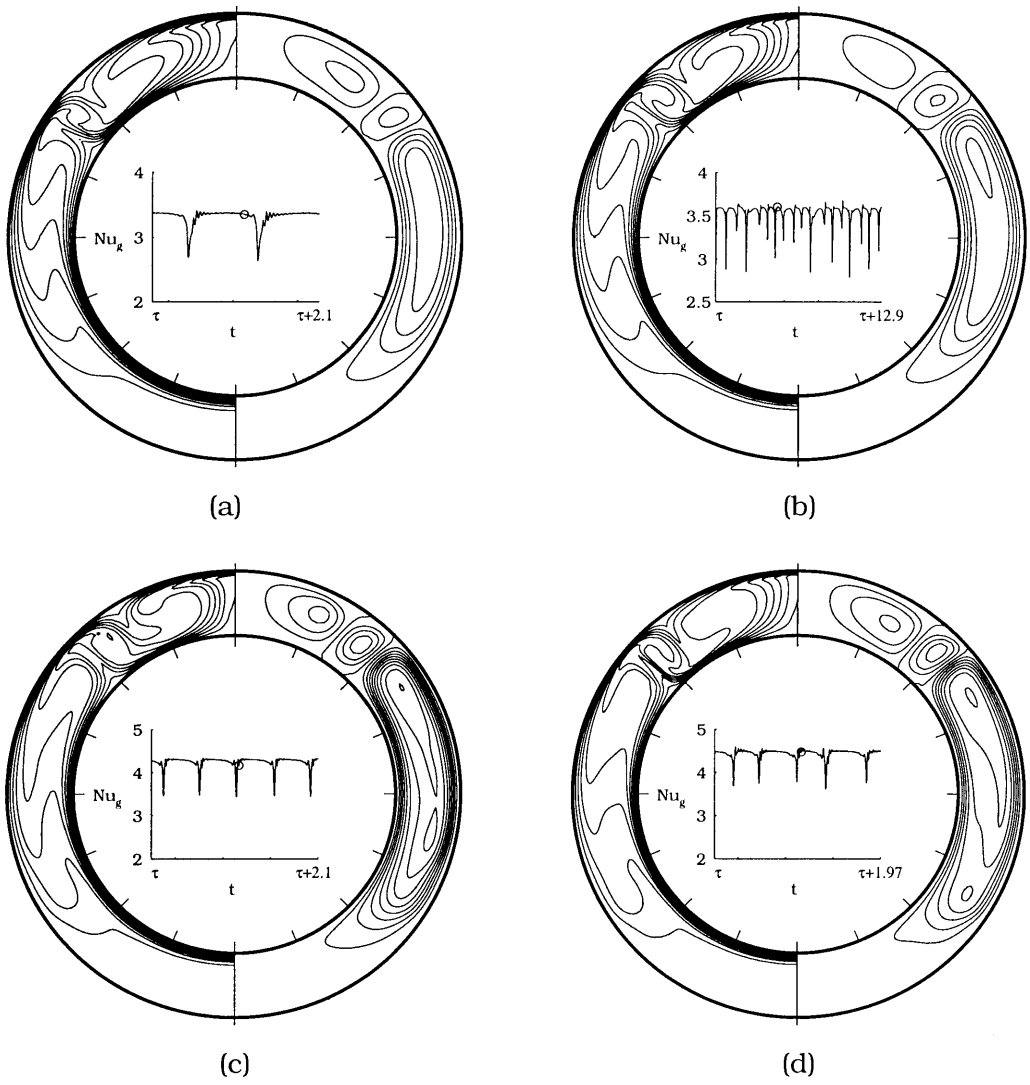

Fig. 7. Flow patterns for $\gamma = 0.4$ and $Gr =$ (a) 1.04×10^5 ($\Delta\psi = -8$); (b) 1.44×10^5 ($\Delta\psi = -8$); (c) 2.88×10^5 ($\Delta\psi = -6.5$); (d) 3.2×10^5 ($\Delta\psi = -8$).

(Fig. 9(a)), this increase, shown by segment A through E of the Nu_g curve, is due to four different multicellular flow structures. Portion AB corresponds to periodic flows that change from four to two cells or from five to three cells, BC the steady five-cell flows, CD the oscillating five-cell flows, and DE the falling vortices flows which change from three cells to one cell within each period. The present curve compares fairly well with that of Scanlan [5], barring the segment A through E. For $\gamma = 0.25$, in addition to the differences in the increased Nu_g region due to changes in the multicellular-flow structure, hysteresis effects also become important, as represented by the two curves marked '2a' and '2b' in Fig. 9(b). Curve 2a represents the reduced heat transfer due to the unicellular flows obtained by decreasing Gr from a steady unicellular solution at $Gr > Gr_r$. Curve 2b represents the higher heat transfer due to the bicellular flows calculated from a solution of curve 1 for $Gr_c < Gr < Gr_r$ as the initial condition. Based on the results shown in Figs 9(a) and (b), it appears that a reverse transition may occur at a Gr where the amplitude of oscillation of Nu_g becomes so large that the minimum value of Nu_g for a multicellular flow becomes smaller than a corresponding unicellular value. For $\gamma = 0.4$, as noted above, no steady multicellular flows, reverse transitions, or hysteresis are calculated in the range of Gr studied, and the curves in

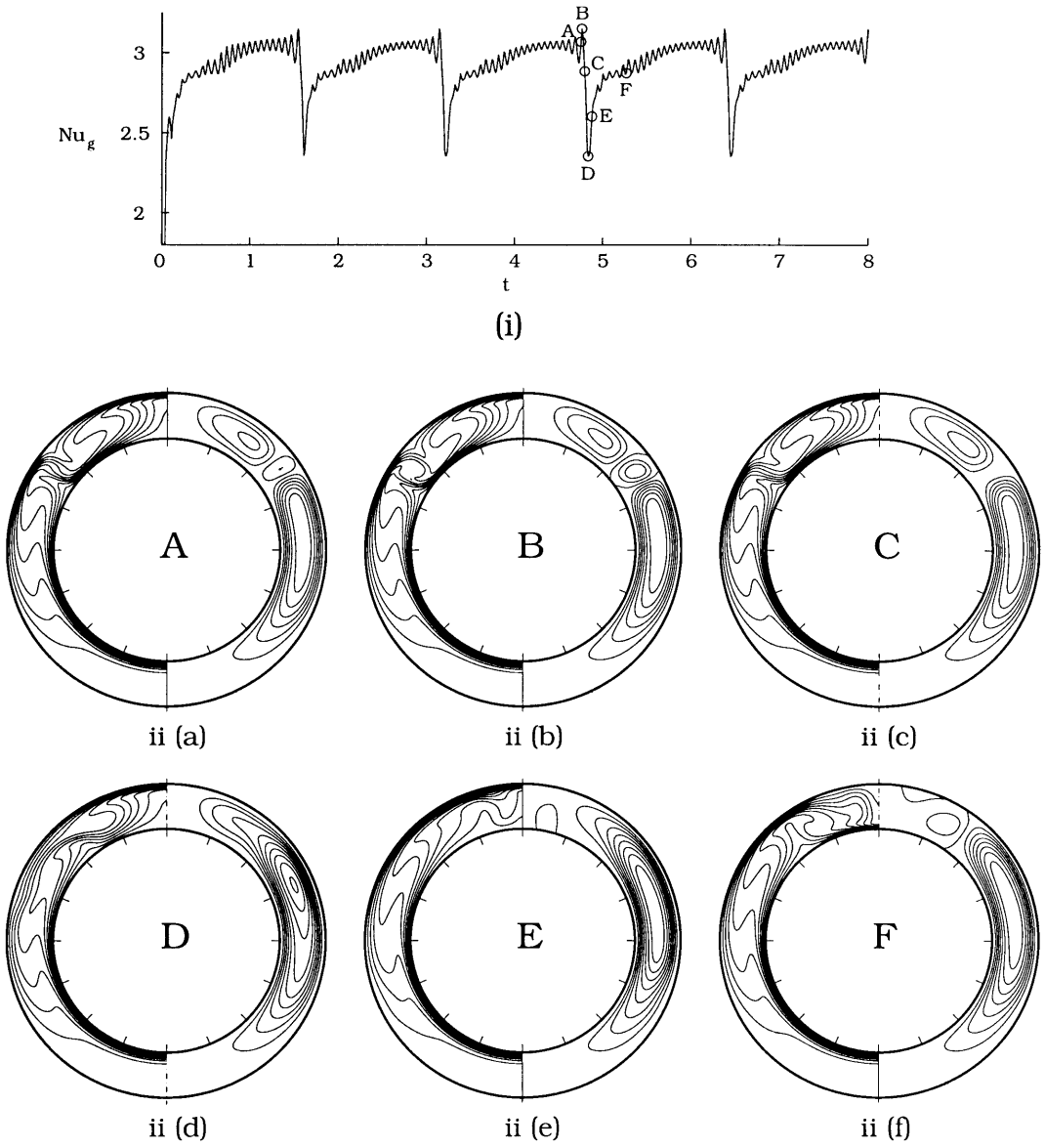

Fig. 8. (i) Nu_g history curve for $Gr = 7.36 \times 10^4$, $\gamma = 0.4$; (ii) flow states corresponding to points A, B, C, D, E, and F of (i).

Fig. 9(c) represent the Nu_g for the steady unicellular and unsteady falling vortices flows only. The waviness of the curves is possibly due to the averaging of Nu_g for the aperiodic flows. Finally, based on the results for these three γs, note that Nu_g increases with Gr for a given γ, and with γ for a given Gr. Though Scanlan's correlation [5] does not show the effects of multicellular flows and hysteresis, the current results suggest no more than about a 30% variation between the Nu_g of the unicellular and the more complex flows.

3.5.2. Local Nusselt numbers

The local heat transfer in the enclosure depends strongly on the flow structure. At low Gr, the isotherms are parallel to the walls and Nu remains almost constant and approximately equal to 1. As Gr increases, Nu changes, the variation depending on θ and γ and, for the unsteady flows, on t as well. For the crescent eddy flows calculated at low Gr, Nu at the inner surface, Nu_i, increases with θ, with the minimum occurring at $\theta = 0$ and the maximum at $\theta = \pi$, due to the increasing temperature gradients. Nu

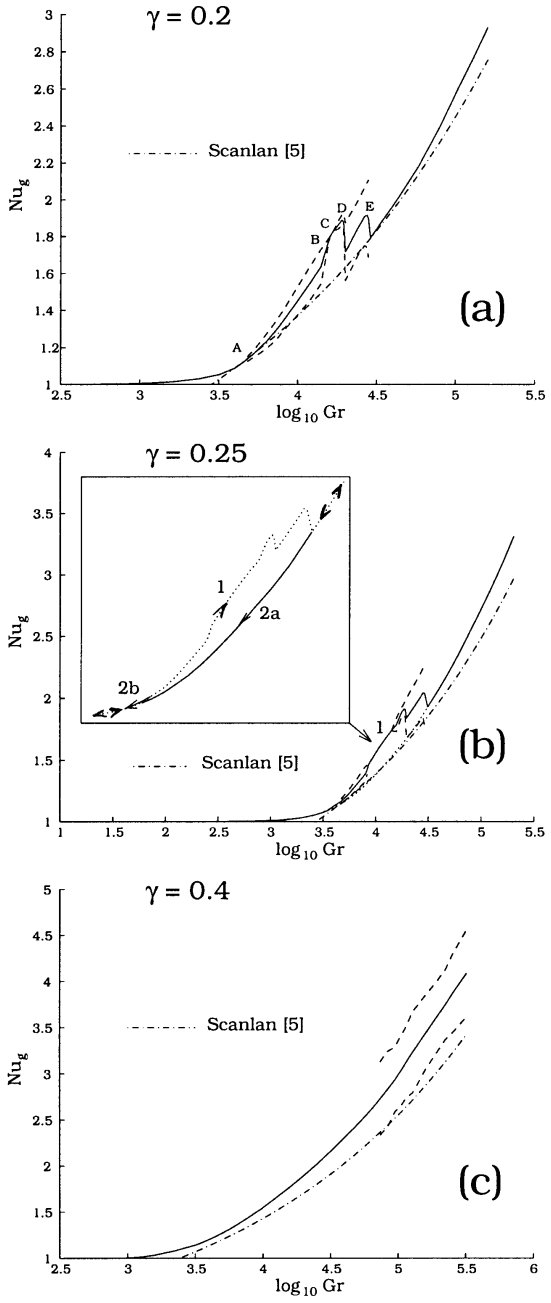

Fig. 9. Variation of Nu_g with Gr for: (a) $\gamma = 0.2$; (b) $\gamma = 0.25$; (c) $\gamma = 0.4$.

at the outer surface, Nu_o, conversely, decreases with θ, the maximum and minimum occurring at $\theta = 0$ and π, respectively. For a given Gr, increasing γ strengthens this trend, as shown in Fig. 10(i–a) for $\gamma = 0.2$, 0.25, and 0.4, at $Gr = 2 \times 10^3$. The influence of steady and oscillatory multicellular flows on Nu is shown in Figs 10(i–(b–d)). Figure 10(i–b) shows the variation of Nu with θ for $\gamma = 0.25$, and $Gr = 14.06 \times 10^3$; one peak and one valley occur at each surface due to the crowding and spreading of the isotherms corresponding to the calculated steady tricellular flow structure. For the oscillatory flows, Nu becomes a function of t also, as illustrated in Fig. 10(i–c) for $\gamma = 0.2$ and $Gr = 9.6 \times 10^3$. The solid curves are the envelopes of the maximum and minimum values of Nu in time, over a period; a typical instantaneous distribution is shown by the dashed line. Its waviness reflects the presence of the multiple cells in the flow and it evolves in time as a traveling wave propagating in the θ-direction. While Nu in the bottom part of the annulus is almost unaffected, large fluctuations in Nu occur in the upper part, demonstrating the effect of the oscillatory multicellular flows. Due to the continuously changing motion, thorough mixing occurs in this region, enhancing the heat transfer compared to that for the unicellular flows. The largest fluctuation occurs close to $\theta = 0$ corresponding to the change in number of cells and their direction of rotation. For instance, while a clockwise-rotating cell at the top causes a higher Nu_o and lower Nu_i, a counter-clockwise rotating cell produces a higher Nu_i and a lower Nu_o. Finally, Fig. 10(i–d) shows the distribution of Nu for a typical falling vortices flow for $\gamma = 0.4$, and $Gr = 6.4 \times 10^4$.

Fig. 10(ii) shows the local Nu distributions for $\gamma = 0.25$, corresponding to a Gr subject to multiple solutions; first, a steady tricellular solution (Fig. 10(ii–a)) for quiescent initial conditions, and second, a unicellular solution (Fig. 10(ii–b)) for a flowing initial condition, each for $Gr = 1.33 \times 10^4$, similar to that described previously. Enhancement of Nu occurs due to crowding of the isotherms for the tricellular flow, illustrating the impact initial conditions may have on the local heat transfer and thus, the global heat transfer.

4. Summary and discussion

Through an axisymmetric transient numerical computation, the temporal evolution of buoyancy driven flows in a spherical annulus are calculated here in detail. The flows and heat transfer corresponding to moderately supercritical Gr were calculated for $Pr = 0.7$ and $\gamma = 0.2$, 0.25, and 0.4.

At low Gr, there is a steady unicellular flow with a $Nu_g \approx 1$; there is always a flow, no matter how small Gr is. As Gr increases, Nu_g increases smoothly for all three γs considered. For $\gamma = 0.2$ and 0.25, this increase is about 10–20% before a change of slope occurs corresponding to the onset of multicellular convection. For $\gamma = 0.4$, Nu_g reaches a value of about 2.75 even before the occurrence of multicellular flows, suggesting that the onset of convection, defined as when Nu_g begins to assume values

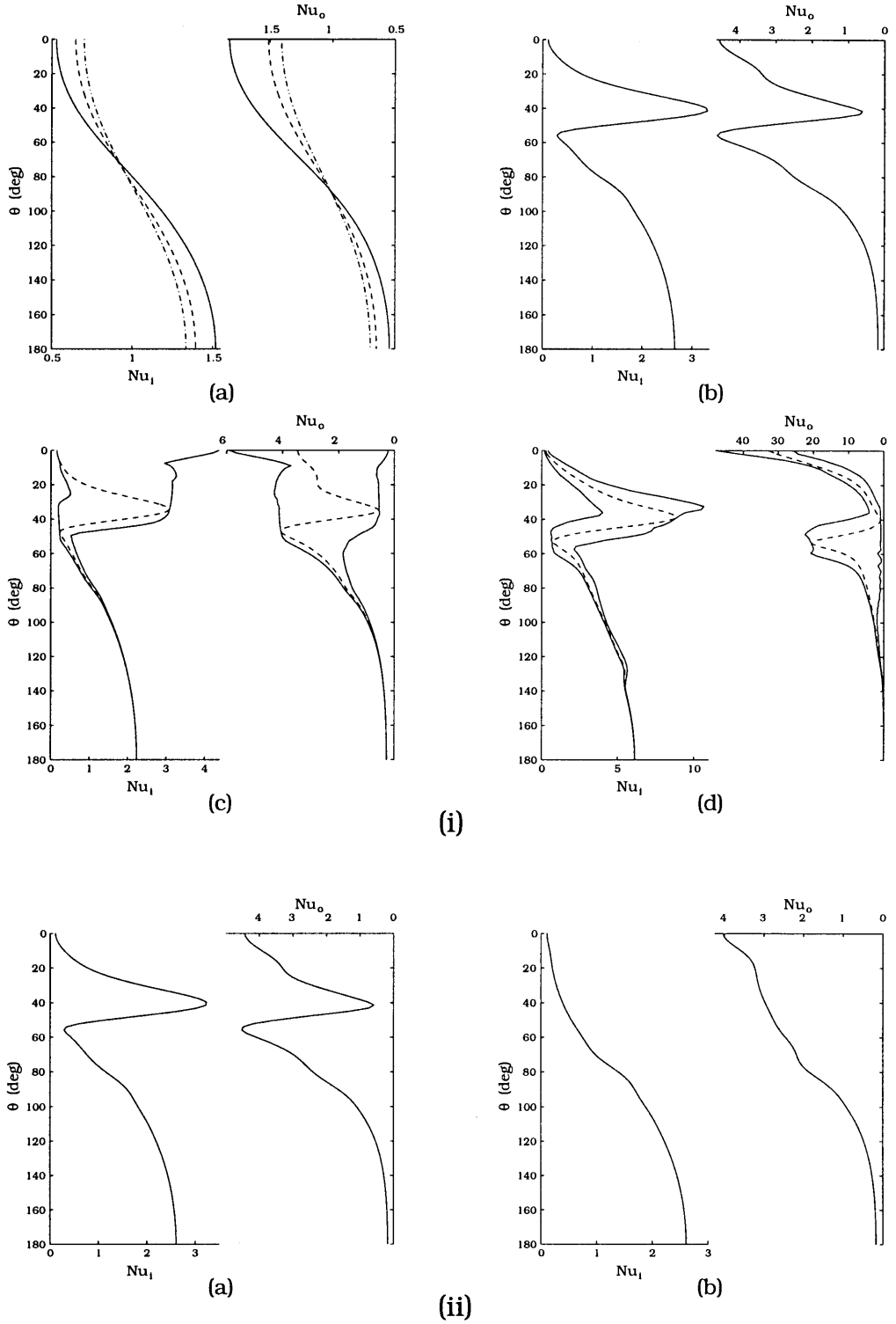

Fig. 10. (i) Variation of *Nu* for: (a) $Gr = 2 \times 10^3$ (solid line: $\gamma = 0.4$; dashed line: $\gamma = 0.25$; chain dotted line: $\gamma = 0.2$); (b) $Gr = 14.063 \times 10^3$, $\gamma = 0.25$; (c) $Gr = 9.6 \times 10^3$, $\gamma = 0.2$. (d) $Gr = 6.4 \times 10^4$, $\gamma = 0.4$. (The solid lines in (c) and (d) are Nu_{max} and Nu_{min}. The dashed line is a typical instantaneous *Nu* distribution.) (ii) Variation of *Nu* for $Gr = 1.33 \times 10^4$, $\gamma = 0.25$ corresponding to: (a) steady tricellular flows; (b) steady unicellular flows.

greater than unity, may not necessarily be the same as that of multicellular convection, especially for higher values of γ. For small values of γ, however, these nearly coincide (unpublished results). The results here suggest that for $\gamma = 0.2$ and 0.25, secondary flows originate near the vertical axis and propagate in θ with increasing Gr or increasing time (for the unsteady flows) and are generally confined to the top one-third of the annulus. For these γs, the region around the vertical axis of a spherical annulus locally resembles the central region of a circular container of small aspect ratios and the fluid in that region is likely to undergo changes in the flow pattern and heat transfer similar to those typically produced in a circular container as a result of the Rayleigh instability. Shear flows occurring due to the spherical geometry further effect the flow in this region and possibly play a role in retaining the flow structure in the bottom two-thirds of the annulus as a crescent eddy type, at least for the moderately supercritical Gr.

The critical Gr values corresponding to the onset of multicellular convection $Gr_c = 4.8 \times 10^3$ and 3.7×10^3 for $\gamma = 0.2$ and 0.25, respectively, are similar to those in TeBeest [20], wherein $Gr_c = 2.9 \times 10^3$ and 8.2×10^3 for $\gamma = 0.176$ and 0.25, respectively. For $\gamma = 0.4$, though, the Gr_c value of 6.9×10^4 calculated here differs from that of 7.3×10^3 obtained in TeBeest [20]. At this onset, while the linear theory [20] predicts a steady flow for $\gamma = 0.176$ and an unsteady flow for $\gamma = 0.25$, the present results indicate unsteady and steady flows for $\gamma = 0.2$ and 0.25, respectively. The ranges of Gr over which the falling vortices flows are calculated for $\gamma = 0.2$ and 0.4 here compare favorably with the results from experimental studies for $\gamma = 0.19$ and 0.4, respectively [1–4]. For $\gamma = 0.2$, the range of Gr obtained here is $1.95 \times 10^4 \leqslant Gr < 3.2 \times 10^4$, while Bishop et al. [1–3] obtained a falling vortices flow at $Gr \approx 2.5 \times 10^4$ [18]. Similarly, for $\gamma = 0.4$, while Yin et al. [4] obtained unicellular flows for $Gr < 10^5$ and a falling vortices flow at $Gr \approx 10^5$, falling vortices flows are calculated here for $6.9 \times 10^4 \leqslant Gr \leqslant 3.2 \times 10^5$. Other flows computed here for $Gr > Gr_c$ are both steady and unsteady for $\gamma = 0.2$ and 0.25, while for $\gamma = 0.4$, these are only unsteady falling vortices flows. There has been apparently only one other study of flows for the supercritical Gr [11]. Ingham [11] calculated only steady unicellular flows for $\gamma = 0.19$ over the range of Gr considered, including Gr for which Bishop et al. [1–3] reported the unsteady falling vortices flows. Representative computations performed for $\gamma = 0.19$ using the present code indicate the occurrence of both steady and unsteady multicellular flows.

The multicellular flows clearly cause enhanced local and global heat transfer. The steady multicellular flows cause steady maxima and minima of temperature gradients in the top portion of the annulus, causing increased or decreased local heat transfer, respectively, at those points on the spherical surfaces all around the periphery. Oscillating multicellular flows, conversely, cause thorough mixing in each period, and hence enhance heat transfer across the entire upper half, instead of causing locally higher heat transfer rates. Since the secondary cells occur only in the upper half, the local heat transfer remains similar to that for unicellular flows in the bottom half. The increase in the global heat transfer, though small, is appreciable, contrary to the conclusions that Nu_g is relatively insensitive to the flow pattern [19].

The reverse transitions from the falling vortices flows to unicellular flows appear to occur due to the increasing influence of the stabilizing temperature gradients in the core, which also leads to a boundary-layer type flow structure. Though this is the first time such reverse transitions are reported in spherical annuli, they have been reported in vertical cylindrical annuli [23], tall vertical cavities [27–31], and spherical annular sectors [24]. Hysteresis following the reverse transition in the spherical annuli appears to be dependent on γ, since no hysteresis was found for $\gamma = 0.2$, while a second set of solutions was found for $\gamma = 0.25$ on the reverse path of the hysteresis-loop. The solutions on the reverse path for the tall vertical enclosures of aspect ratio 16 and $Pr = 0.71$ being composed of both uni- and multicellular flows [27, 28], as opposed to the steady unicellular flows in the present investigation and the spherical annular sectors [24] for $\gamma = 0.25$, demonstrates the effect of geometry on such flows. Finally, for $\gamma = 0.4$, the unsteady solutions calculated appear to be essentially of the same nature as those found in the experiments of Yin et al. [4], though lacking the spiral motion noted during mixing of the cells in the latter, possibly due to the ideal axisymmetry assumed here.

5. Conclusions

The solutions for the buoyancy induced laminar flows in spherical annuli presented here demonstrate the effect of the flow structures on heat transfer. It is shown that the multicellular flows can cause the overall heat transfer to increase by as much as 30% (depending on γ), with significant changes in the local heat transfer. For $\gamma = 0.2$ and 0.25, the transition from the crescent eddy to falling vortices flows is not direct, as suggested by earlier studies, but occurs after a series of steady and unsteady multicellular regimes for intermediate Gr. Moreover, the falling vortices regime disappears at a critical Gr giving rise to steady unicellular flows which display characteristics of the boundary layer regime. This reverse transition to unicellular flows for $\gamma = 0.25$ is characterized by hysteresis, such that for any Gr within the two transitions, one of two dissimilar flows may occur. Experimentally and in design, this would mean that the flows obtained by steadily increasing Gr (or ΔT^*) to some required value

could entail different heat transfer rates, both locally and globally, as compared to those obtained by first increasing Gr beyond the transition values, and then decreasing it to the desired value. Further, the local extrema in Nu calculated for the steady multicellular flows indicates the presence of locally high heat flux areas, as opposed to the periodically varying Nu for the oscillatory flows which cause more uniform heat flux distribution in the entire upper region over a period, though both types of flows may yield approximately the same Nu_g. Accordingly, care must be exercised to maintain operation in the appropriate range of Gr in design applications for which local heat transfer is important, instead of proceeding solely on the values of Nu_g. Finally, reverse transitions may not always be associated with hysteresis, depending on the value of γ.

References

[1] E.H. Bishop, R.S. Kolflat, L.R. Mack, J.A. Scanlan, Convective heat transfer between concentric spheres. Proceedings of Heat Transfer and Fluid Mechanics Institute, Stanford University Press, 1964. pp. 69–80.

[2] E.H. Bishop, R.S. Kolflat, L.R. Mack, J.A. Scanlan, Photographic studies of convection patterns between concentric spheres, Soc. Photo-Optical Instrumentation Engrs Jl 3 (1964–1965) 47–49.

[3] E.H. Bishop, L.R. Mack, J.A. Scanlan, Heat transfer by natural convection between concentric spheres, Int. J. Heat Mass Transfer 9 (1966) 649–662.

[4] S.H. Yin, R.E. Powe, J.A. Scanlan, E.H. Bishop, Natural convection flow patterns in spherical annuli, Int. J. Heat Mass Transfer 16 (1973) 1785–1795.

[5] J.A. Scanlan, E.H. Bishop, R.E. Powe, Natural convection heat transfer between concentric spheres, Int. J. Heat Mass Transfer 13 (1970) 1857–1872.

[6] R.J. Brown, Natural convection between concentric spheres. PhD dissertation, University of Texas, Austin, 1967.

[7] L.R. Mack, H.C. Hardee, Natural convection between concentric spheres at low Rayleigh numbers, Int. J. Heat Mass Transfer 11 (1968) 387–396.

[8] S.N. Singh, J. Chen, Numerical solution for free convection between concentric spheres at moderate Grashof numbers, Numerical Heat Transfer 3 (1980) 441–459.

[9] K.N. Astill, H. Leong, R. Martorana, A numerical solution for natural convection in concentric spherical annuli. In Natural Convection in Enclosures, ASME, 1980. pp. 105–13.

[10] J.P. Caltagirone, M. Combarnous, A. Mojtabi, Natural convection between concentric spheres: transition towards a multicellular flow, Numerical Heat Transfer 3 (1980) 107–114.

[11] D.B. Ingham, Heat transfer by natural convection between spheres and cylinders, Numerical Heat Transfer 4 (1981) 53–67.

[12] S.N. Singh, J.M. Elliot, Natural convection between concentric spheres in a slightly thermally stratified medium, Int. J. Heat Mass Transfer 24 (1981) 395–406.

[13] J. Nelson, R. Douglass, D. Alexander, Natural convection in a spherical annulus filled with heat generating fluid. Proceedings of 9th International Heat Transfer Conference. Vol. 2. 1982. p. 171–6.

[14] A. Mojtabi, J.P. Caltagirone, Natural convection between two concentric spheres for high Prandtl number, Proceedings of 7th International Heat Transfer Conference, Munich, Vol. 2. New York: Hemisphere, 1982. p. 245–9.

[15] J.M. Nelson, R.W. Douglass, Non-uniform energy generation effects on natural convection in a spherical annulus enclosure, Int. J. Heat Mass Transfer 27 (1984) 1928–1932.

[16] T. Fujji, T. Honda, M. Fujji, A numerical analysis of laminar free convection around an isothermal sphere: finite difference solution of the full Navier–Stokes and energy equations between concentric spheres, Numerical Heat Transfer 7 (1984) 103–111.

[17] J.L. Wright, R.W. Douglass, Natural convection in narrow-gap, spherical annuli, Int. J. Heat Mass Transfer 29 (1986) 725–739.

[18] R.W. Douglass, K.G. TeBeest, S.A. Trogdon, D.R. Gardner, Prandtl number effects on the stability of natural convection between spherical shells, Int. J. Heat Mass Transfer 33 (1990) 2533–2544.

[19] D.R. Gardner, R.W. Douglass, S.A. Trogdon, Linear stability of natural convection in spherical annuli, J. Fluid Mech. 126 (1990) 91–121.

[20] K.G. TeBeest, Linear stability and bifurcation of natural convection within arbitrary-gap spherical annuli. Ph.D. dissertation, University of Nebraska—Lincoln, Lincoln, Nebraska, 1992.

[21] V.K. Garg, Natural convection between concentric spheres, Int. J. Heat Mass Transfer 35 (1992) 1935–1945.

[22] H. Chu, T. Lee, Transient natural convection heat transfer between concentric spheres, Int. J. Heat Mass Transfer 36 (1993) 3159–3170.

[23] C.P. Chiu, W.R. Chen, Transient natural convection heat transfer between concentric and vertically eccentric spheres, Int. J. Heat Mass Transfer 39 (1996) 1439–1452.

[24] C. Thamire, N.T. Wright, Buoyancy induced flows in spherical annular sectors: a numerical study, Numerical Heat Transfer 33 (1998) 107–130.

[25] P.J. Roache, Computational Fluid Mechanics, 6th ed. Albuquerque, Hermosa, 1992.

[26] P. Le Quéré, J. Pécheux, Numerical simulations of multiple flow transitions in axisymmetric annulus convection, J. Fluid Mech. 206 (1989) 517–544.

[27] P. Le Quéré, A note on multiple and unsteady solutions in two-dimensional convection in a tall cavity, ASME J. Heat Transfer 112 (1990) 965–974.

[28] S. Watikani, Development of multicellular solutions in natural convection in an air-filled vertical cavity, ASME J. Heat Transfer, Trans. ASME 119 (1997) 97–101.

[29] P. Roux, J. Grandin, P. Bontoux, G. de Vaul Davis, Reverse transition from multicellular to monocellular motion in vertical fluid layer, Phys. Chem. Hydro. 3 (F) (1980) 292–297.

[30] G. Lauriat, G. Desrayaud, Natural convection in air-filled cavities of high aspect ratios: discrepancies between experimental and theoretical results; ASME Paper No. 85-HT - 37, 1985.

[31] A. Chikhaoui, J.F. Marcillat, R.L. Sani, Successive transitions in thermal convection in a vertical rectangular enclosure. In: Natural Convection in Enclosures, ASME HTD—Vol. 99, 1988. p. 29–35.

[32] C. Thamire, Buoyancy driven flows and heat transfer in spherical annular enclosures. PhD dissertation, The University of Maryland, Baltimore County, Baltimore, Maryland, 1997.